Effect of 3-D viscoelastic structure on post-seismic relaxation from the 2004 $M = 9.2$ Sumatra earthquake

Fred Pollitz,[1] Paramesh Banerjee,[2] Kelly Grijalva,[3] B. Nagarajan[4] and R. Bürgmann[3]

[1] *U.S. Geological Survey, Menlo Park, CA 94025, USA. E-mail: fpollitz@usgs.gov*
[2] *Wadia Institute of Himalayan Geology, Dehradun, India*
[3] *Department Earth and Planetary Sci., UC Berkeley, CA 94720, USA*
[4] *Geodetic and Research Branch, Survey of India, Dehradun, India*

SUMMARY
The 2004 $M = 9.2$ Sumatra–Andaman earthquake profoundly altered the state of stress in a large volume surrounding the $\sim$1400 km long rupture. Induced mantle flow fields and coupled surface deformation are sensitive to the 3-D rheology structure. To predict the post-seismic motions from this earthquake, relaxation of a 3-D spherical viscoelastic earth model is simulated using the theory of coupled normal modes. The quasi-static deformation basis set and solution on the 3-D model is constructed using: a spherically stratified viscoelastic earth model with a linear stress–strain relation; an aspherical perturbation in viscoelastic structure; a 'static' mode basis set consisting of Earth's spheroidal and toroidal free oscillations; a "viscoelastic" mode basis set; and interaction kernels that describe the coupling among viscoelastic and static modes. Application to the 2004 Sumatra–Andaman earthquake illustrates the profound modification of the post-seismic flow field at depth by a slab structure and similarly large effects on the near-field post-seismic deformation field at Earth's surface. Comparison with post-seismic GPS observations illustrates the extent to which viscoelastic relaxation contributes to the regional post-seismic deformation.

Key words: Numerical solutions; Continental margins: convergent; Dynamics of lithosphere and mantle; Rheology: mantle.

GJI Seismology

1 INTRODUCTION

The 2004 $M = 9.2$ Sumatra–Andaman earthquake is the largest earthquake to have occurred globally since 1964 and involved the longest rupture ($\sim$1400–1500 km) of any known historic earthquake (Meltzner *et al.* 2006). The earthquake produced measurable static displacements up to 5000 km away (Banerjee *et al.* 2005). The large coseismic stress changes in concert with a ductile asthenosphere are expected to produce a substantial post-seismic velocity field. Observed post-seismic surface velocities for the first few months are up to 600 mm yr^{-1}, about 10 times greater than background velocities (Apel *et al.* 2006), and can be explained with asthenosphere relaxation governed by a transient rheology (Pollitz 2003b; Pollitz *et al.* 2006a). Three-dimensional (3-D) rheology structure, particularly that associated with a descending slab, can substantially influence coseismic and post-seismic relaxation fields (Masterlark 2003; Hu *et al.* 2004). Tangible post-seismic relaxation from the 2004 Sumatra earthquake may persist for decades to come, based on observations made decades after the similar-sized 1960 Chilean earthquake (Hu *et al.* 2004) and 1964 Alaska earthquake (Cohen 1996). In this paper, we investigate the effects of 3-D viscoelastic structure on the early ($\sim$first-year) post-Sumatra mantle flow fields and surface velocity fields, and we compare forward models with available post-seismic GPS observations.

2 COUPLED NORMAL MODE SOLUTION

2.1 Decomposition into static and viscoelastic normal modes

Static and post-earthquake relaxation are governed by the equations of quasi-static equilibrium (e.g. Appendix B of Pollitz 2003a). We approach the problem of static and post-earthquake deformation on a 3-D viscoelastic earth model using a solution of these equations based on coupled normal modes (Pollitz 2003a). This solution is constructed using a basis set of 'viscoelastic' modes S^{VE} and 'static' modes S^{static} defined on a reference spherically symmetric earth model $\mathbf{m}^0$. We assume that $\mathbf{m}^0$ consists of a distribution of isotropic elastic parameters $\{\kappa_0(r), \mu_0^{(1)}(r)\}$, where $\kappa_0(r)$ and $\mu_0^{(1)}(r)$ are, respectively, bulk and shear modulus as a function of radius r; density $\rho_0(r)$; viscosities $\{\eta_0^{(k)}(r) \mid k \geq 1\}$ and auxiliary shear moduli $\{\mu_0^{(k)}(r) \mid k \geq 2\}$. We assume a linearized stress–strain relation that could describe a generalized Burgers body (Ivins 1996). In present applications we shall consider a Maxwell rheology, which requires only one viscosity $\eta_0^{(1)}(r)$ and shear modulus $\mu_0^{(1)}(r)$, or a Burgers body, which requires one additional viscosity $\eta_0^{(2)}(r)$ and one additional shear modulus $\mu_0^{(2)}(r)$ to describe the Kelvin element of the rheology (e.g. Ivins 1996; Pollitz 2003a).

On a spherically symmetric viscoelastic structure, S^{VE} represents the post-earthquake motions, and S^{static} represents the final static displacement field on the elastic part of $\mathbf{m}^0$ using Earth's free oscillations, that is, the deformation field after cessation of seismic wave propagation but before relaxation of the ductile components of $\mathbf{m}^0$. This decomposition is possible because inertial terms are neglected in the equations of quasi-static equilibrium. However, it assumes a complete decoupling between the processes of seismic wave attenuation and post-earthquake relaxation. This restriction is not necessary to implement the Pollitz (2003a) solution. The static modes and viscoelastic modes could be unified into a single viscoelastic mode that embodies the combined effects of seismic wave propagation, attenuation and subsequent relaxation (Yuen & Peltier 1982). We proceed here with the decomposition into static and viscoelastic modes in order to avoid the complications associated with coupling seismic wave attenuation with long-term viscoelastic relaxation.

2.2 Displacement field

We shall work throughout in the Laplace transform domain. The Laplace transform of a function $f(t)$ with independent variable s is

$$\tilde{f}(s) = L[f(t)] = \int_0^\infty f(t)\exp(-st)\,dt. \tag{1}$$

Working in $r - \theta - \phi$ spherical coordinates, the displacement field on the spherically symmetric earth model $\mathbf{m}^0$ takes the form

$$\tilde{\mathbf{u}}^0(\mathbf{r};s) = \sum_{j\in\mathbf{S}} \mathbf{O}^j(\mathbf{r})\Phi_j^0(\hat{\mathbf{r}};s), \tag{2}$$

where $\tilde{\mathbf{u}}^0(\mathbf{r};s)$ is the Laplace-transformed displacement at point $\mathbf{r}$; $\Phi_j^0(\hat{\mathbf{r}};s)$ is a potential function associated with the jth normal mode ($\hat{\mathbf{r}} = \mathbf{r}/r$ is the position on the unit sphere); $\mathbf{O}^j(\mathbf{r})$ is the vector differential operator

$$\mathbf{O}^j(\mathbf{r}) = -W_j(r)\hat{\mathbf{r}}\times\nabla_1 + U_j(r)\hat{\mathbf{r}} + V_j(r)\nabla_1, \tag{3}$$

where

$$\nabla_1 = \frac{\partial}{\partial\theta}\hat{\theta} + (\sin\theta)^{-1}\frac{\partial}{\partial\phi}\hat{\phi} \tag{4}$$

is the surface gradient operator, W_j is the toroidal-mode radial eigenfunction, and U_j and V_j are the vertical and horizontal spheroidal-mode radial eigenfunctions, respectively. Thus W_j is non-zero for a toroidal mode, and U_j and V_j are non-zero for a spheroidal mode. The summation over j in eq. (2) is over the combined set of viscoelastic and static modes $\mathbf{S} = \mathbf{S}^{VE} \cup \mathbf{S}^{static}$. Expressions for $\Phi_j^0(\hat{\mathbf{r}};s)$ for excitation by a moment tensor or a directed force are given in Appendix A of Pollitz (2003a).

Since a spherical harmonic expansion is used to represent the solution eq. (1), each $\Phi_j^0(\hat{\mathbf{r}};s)$ is accociated with a definite spherical harmonic degree, denoted by l_j. Each $\Phi_j^0(\hat{\mathbf{r}};s)$, therefore, satisfies the 2-D Helmholz equation on a spherical membrane

$$\nabla_1^2\Phi_j^0(\hat{\mathbf{r}};s) + l_j(l_j+1)\Phi_j^0(\hat{\mathbf{r}};s) = 0. \tag{5}$$

The function $\tilde{\mathbf{u}}^0(\mathbf{r};s)$ has simple poles at $s = 0$ and $s = -s_j$ for a set $\{s_j \mid j \in \mathbf{S}^{VE}\}$. Each $s_j > 0$ is associated with a solution of the equations of static equilibrium on $\mathbf{m}^0$ for spherical harmonic degree l_j; for a fixed spherical harmonic degree there are generally several such solutions (e.g. Pollitz 1997). For a source that acts as a step function in time, the j-component $\tilde{\mathbf{u}}^0(\mathbf{r};s)$ behaves as $\sim s^{-1}\Psi_j(s)$

where (eq. 7 of Pollitz 2003a)

$$\Psi_j(s) = \begin{cases} 1 & j \in \mathbf{S}^{static} \\ \frac{1}{s+s_j} & j \in \mathbf{S}^{VE} \end{cases}. \tag{6}$$

In the time domain, we therefore, have

$$\mathbf{u}^0(\mathbf{r},t) \sim \begin{cases} H(t) & j \in \mathbf{S}^{static} \\ \frac{H(t)}{s_j}[1 - \exp(-s_jt)] & j \in \mathbf{S}^{VE} \end{cases}, \tag{7}$$

where $H(t)$ is the Heaviside step function.

We define a 3-D earth model $\mathbf{m}$ as

$$\mathbf{m} = \left\{\kappa(\mathbf{r}), \mu^{(1)}(\mathbf{r}), \rho(\mathbf{r})\right\} \cup \left\{\eta^{(k)}|k \geq 1\right\} \cup \left\{\mu^{(k)}(\mathbf{r})|k \geq 2\right\}. \tag{8}$$

The last two sets in eq. (8) contain perturbations in the non-elastic components of the rheology structure. Because the stress–strain relation is linear, and assuming no bulk relaxation, these perturbations may be absorbed into the s-dependent shear modulus in the Laplace transform domain. Then $\tilde{\mathbf{u}}^0(\mathbf{r};s)$ obeys the equations of quasi-static equilibrium with perturbations in elastic parameters and shear modulus given by (Appendix B of Pollitz 2003a)

$$\delta\kappa(\mathbf{r}) = \kappa(\mathbf{r}) - \kappa_0(r)$$
$$\delta\mu(\mathbf{r},s) = \tilde{\mu}(\mathbf{r},s) - \tilde{\mu}_0(r,s)$$
$$\delta\rho(\mathbf{r}) = \rho(\mathbf{r}) - \rho_0(r), \tag{9}$$

where $\tilde{\mu}$ and $\tilde{\mu}_0$ are the transformed shear moduli on $\mathbf{m}$ and $\mathbf{m}_0$, respectively. The perturbation in μ is thus s-dependent and depends on the 3-D distributions of $\eta^{(k)}$ and $\mu^{(k)}$. For a Burgers body, the rheology on $\mathbf{m}_0$ is described by a Maxwell element with shear modulus $\mu_0^{(1)}$ and viscosity $\eta_0^{(1)}$ and a Kelvin element with shear modulus $\mu_0^{(2)}$ and viscosity $\eta_0^{(2)}$. On $\mathbf{m}$ the rheology is described by parameters $\mu^{(1)}(\mathbf{r}), \eta^{(1)}(\mathbf{r}), \mu^{(2)}(\mathbf{r})$ and $\eta^{(2)}(\mathbf{r})$. The perturbation $\delta\mu(\mathbf{r},s)$ is then given by

$$\delta\mu(\mathbf{r},s) = \frac{\mu^{(1)}(\mathbf{r})s\left[s + \frac{\mu^{(2)}(\mathbf{r})}{\eta^{(2)}(\mathbf{r})}\right]}{\left[\left(s + \frac{\mu^{(2)}(\mathbf{r})}{\eta^{(2)}(\mathbf{r})}\right)\left(s + \frac{\mu^{(1)}(\mathbf{r})}{\eta^{(1)}(\mathbf{r})}\right) + s\frac{\mu^{(1)}(\mathbf{r})}{\eta^{(2)}(\mathbf{r})}\right]}$$
$$- \frac{\mu_0^{(1)}(r)s\left[s + \frac{\mu_0^{(2)}(r)}{\eta_0^{(2)}(r)}\right]}{\left[\left(s + \frac{\mu_0^{(2)}(r)}{\eta_0^{(2)}(r)}\right)\left(s + \frac{\mu_0^{(1)}(r)}{\eta_0^{(1)}(r)}\right) + s\frac{\mu_0^{(1)}(r)}{\eta_0^{(2)}(r)}\right]}. \tag{10}$$

The displacement field on $\mathbf{m}$ takes the form

$$\tilde{\mathbf{u}}(\mathbf{r};s) = \sum_{j\in\mathbf{S}} \mathbf{O}^j(\mathbf{r})\Phi_j(\hat{\mathbf{r}};s) \tag{11}$$

where using eqs (11), (17) and (18) of Pollitz (2003a), the full potential functions obey the set of coupled integral equations

$$\Phi_j(\hat{\mathbf{r}};s) = \Phi_j^0(\hat{\mathbf{r}};s) + \Phi_j^1(\hat{\mathbf{r}};s), \tag{12}$$

where $\Phi_j^1(\hat{\mathbf{r}};s)$ is the aspherical part of the full potential given by

$$\Phi_j^1(\hat{\mathbf{r}};s) = -\Psi_j(s)\frac{2l_j+1}{4\pi}\int_\Gamma d^2\hat{\mathbf{r}}' \sum_{N=0}^2 (-1)^N P_{l_j}^N(\cos\theta)$$
$$\times \sum_{j'} \text{Re}\left\{\delta\omega_{jj'}(\hat{\mathbf{r}}';s)\left(\sqrt{2}H_+\right)^N\right\}\Phi_{j'}(\hat{\mathbf{r}}';s). \tag{13}$$

In eq. (13) the integration is over those $\mathbf{r}' \in \Gamma$ on the unit sphere with aspherical viscoelastic structure. Referring to Fig. 1, θ is the
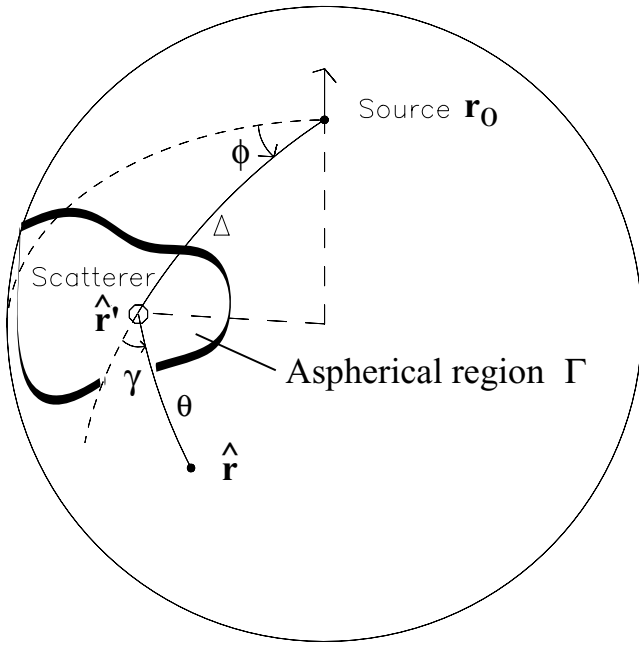
Figure 1. Scattering geometry for scatterer $\hat{\mathbf{r}}'$ to receiver $\hat{\mathbf{r}}$ interactions, with angular distance θ and azimuth γ. From source $\mathbf{r}_0$ to scatterer $\hat{\mathbf{r}}'$, the angular distance and azimuth are Δ and ϕ, respectively. From Pollitz (2003a).

angular distance between the $\mathbf{r}$ and $\mathbf{r}'$; $P_l^N(\cos\theta)$ is an associated Legendre function of degree l and order N defined by $P_l^N(x) = (1 - x^2)^{m/2} \mathrm{d}^m P_l(x)/\mathrm{d}x^m$. The $\delta\omega_{jj'}(\hat{\mathbf{r}}'; s)$ are interaction kernels among the normal modes given in Appendix A of Friederich (1999), and they depend on the perturbations given in eq. (9); the $(\sqrt{2}H_+)^N$ are differential operators with respect to the primed coordinates acting on the potential functions and are prescribed in Appendix D of Friederich (1999); Re{} denotes the real part of the function in brackets. In eq. (13) we assume a normalization convention for the mode eigenfunctions $\epsilon_j = 1$ for all modes j, where ϵ_j is given in eq. (8) of Pollitz (2003a).

From eqs (5), (12) and (13) it follows that the aspherical part of the full potential functions satisfies the 2-D Helmholz equation on a spherical membrane

$$\nabla_1^2 \Phi_j^1(\hat{\mathbf{r}}; s) + l_j(l_j + 1)\Phi_j^1(\hat{\mathbf{r}}; s) = 0. \tag{14}$$

2.3 Numerical solution

A well-known iterative method of solving the set of eqs (12) and (13) is to substitute the current set of potentials $\{\Phi_j(\hat{\mathbf{r}}; s) | j \in \Omega\}$ into the right-hand side of eq. (13), then evaluate eqs (12) and (13) to obtain the updated set of potentials, and so forth. The first iteration is done using the set of potentials on $\mathbf{m}_0\{\Phi_j^0(\hat{\mathbf{r}}; s) | j \in \Omega\}$. This solution assumes that the updated sets of potentials converge to stable final values. This is the case with the examples considered here. An alternative solution which is generally stable, though more computationally demanding, is given by eqs (25) and (26) of Pollitz (2003a).

Within an iteration for which values of the full potentials on Γ are available, the direct evaluation of the surface integrals on the right-hand side of eq. (13) is computationally time consuming. We make use of a representation theorem, first given by Dahlen (1980) and repeated in eqs (31) and (32) of Pollitz (2003a), which follows

from eq. (14). It allows the surface integrals to be recast as line integrals about a closed contour C on the unit sphere:

$$\Phi_j^1(\hat{\mathbf{r}}_0; s)$$
$$= \int_C \left[\Phi_j^1(\hat{\mathbf{r}}; s)\hat{\mathbf{n}} \cdot \nabla_1 G(\hat{\mathbf{r}}, \hat{\mathbf{r}}_0; l_j) - G(\hat{\mathbf{r}}, \hat{\mathbf{r}}_0; l_j)\hat{\mathbf{n}} \cdot \nabla_1 \Phi_j^1(\hat{\mathbf{r}}; s) \right] d\mathbf{l}, \tag{15}$$

where $d\mathbf{l} = |d\hat{\mathbf{r}}|$ is the length element and $G(\hat{\mathbf{r}}, \hat{\mathbf{r}}_0; l)$ satisfies

$$\nabla_1^2 G(\hat{\mathbf{r}}, \hat{\mathbf{r}}_0; l) + l(l+1)G(\hat{\mathbf{r}}, \hat{\mathbf{r}}_0; l) = \delta(\hat{\mathbf{r}}, \hat{\mathbf{r}}_0), \tag{16}$$

where $\delta(\hat{\mathbf{r}}, \hat{\mathbf{r}}_0)$ is the Dirac δ-function. Remarkably, C can be *any* closed contour on the unit sphere, although the singular behaviour of G for $\hat{\mathbf{r}}$ near $\hat{\mathbf{r}}_0$ is practically handled by choosing a contour that just surrounds Γ. One need only note that $\hat{\mathbf{r}}_0$ in eq. (15) is to be regarded as 'inside' C. For a given $\hat{\mathbf{r}}_0$ this determines the spherical surface inside C and that outside C, and $\hat{\mathbf{n}}$ is then prescribed to be the local unit vector, tangent to the sphere, pointing towards the spherical surface outside C. This provides us with an efficient scheme to update the set of potentials $\Phi_j(\hat{\mathbf{r}}; s)$ from iteration i to iteration $i + 1$. With sufficiently fine discretization of Γ and C, this is accomplished in two steps: first, using eqs (12) and (13), with $\Phi_j(\hat{\mathbf{r}}; s)$ from iteration i, to evaluate updated $\Phi_j(\hat{\mathbf{r}}; s)$ for $\hat{\mathbf{r}} \in C$; second, using eqs (12) and (15), with the updated $\Phi_j(\hat{\mathbf{r}}; s)$ on C, to evaluate the updated $\Phi_j^1(\hat{\mathbf{r}}_0; s)$ for $\hat{\mathbf{r}}_0 \in \Gamma$. As explained in Section 3.3 of Pollitz (2003a), this results in a computation time of the potential functions on the 3-D structural model that is proportional to the volume over which the aspherical part of $\mathbf{m}$ is non-zero times the number of mode branches M used in the spherical harmonic expansion of the wavefield. For a truncated spherical harmonic expansion, this may be thought of as being proportional to the area A of Γ times the length of C (which scales as $\sqrt{A}$) times M.

The integrations in eq. (13) require the values of up to second horizontal spatial derivatives of the potential functions. Through eq. (15) this requires, in turn, the values of up to third horizontal spatial derivatives of spherical harmonics $[P_l^N(\cos\theta)] \times \exp(iN\gamma)$ with respect to changes in running coordinates of points $\mathbf{r}' \in C$. In computations we use analytic expressions for these spatial derivatives. They have been checked against numerically determined derivatives, and the validity of eq. (15) has been checked for each individual spherical harmonic component (Appendix A).

3 SYNOPSIS OF APPROACH

Post-earthquake relaxation of a 3-D viscoelastic earth model is simulated using the theory of coupled viscoelastic modes and Earth's free oscillations based on eqs (11) and (12). We note that iterative solution of the set of coupled integral eq. (12) is a generally powerful way of synthesizing the effect of aspherical structure in elastic-wave, static or quasi-static problems. A similar approach (using direct Greens functions rather than normal modes) is used by Du *et al.* (1994) to evaluate static deformation in the presence of 3-D rigidity variations. In seismic wave propagation, essentially the same equation—eq. (34) of Friederich (2003)—was used as the basis for seismic tomography of the east Asian mantle using fully 3-D sensitivity kernels. In the post-earthquake case, the solution for quasi-static deformation is constructed using the following elements.

(1) A spherically stratified viscoelastic earth model $\mathbf{m}_0$. (A linear stress–strain relation is assumed.)
(2) An aspherical perturbation in viscoelastic structure $\delta\mathbf{m}$.

(3) A 'static' mode basis set S^{static} consisting of Earth's spheroidal and toroidal free oscillations, including the fundamental mode and first n overtones, truncated at a maximum spherical harmonic degree of l_{max}.

(4) A 'viscoelastic' mode basis set S^{VE} consisting of all spheroidal and toroidal viscoelastic modes truncated at a maximum spherical harmonic degree of l_{max}.

(5) Interaction kernels that describe the coupling of all viscoelastic and static modes with one another under the aspherical perturbation $\delta\mathbf{m}$.

(6) A representation theorem that recasts the surface integrals in eq. (12) as line integrals along a contour surrounding the region of aspherical structure.

The set of integral equations for the system of coupled potentials is discretized and solved in the Laplace transform domain. A numerical inverse Laplace transform is used to produce time domain results.

The mode-based solution of post-earthquake relaxation on an aspherical viscoelastic structure has several noteworthy properties:

(1) It is semi-analytic.

(2) Both the number of overtones n and the maximum spherical harmonic degree l_{max} are, in principle, unbounded but are chosen practically according to the length scales demanded by the problem. A larger l_{max} corresponds to deformation of shorter horizontal wavelength, and a larger n corresponds to deformation of shorter vertical wavelength.

(3) The solution of the coupled integral equations is obtained through summation of the Born series. It is globally valid, even when the aspherical structure is defined over a limited volume. A greater number of iterations is required the larger the magnitude or spatial extent of the aspherical viscoelastic structure.

(4) The effect of aspherical structure on the static displacement field (initial coseismic displacement field at time $t = 0$) is embodied in S$^{static} \to$ S^{static} coupling. The effect of aspherical structure on the post-earthquake relaxation fields ($t > 0$) is embodied in all possible coupling configurations, that is, S$^{static} \to$ S^{static}, S$^{static} \to$ S^{VE}, S$^{VE} \to$ S^{static}, and S$^{VE} \to$ S^{VE}.

(5) The computational effort is proportional to the volume of the aspherical region.

4 EXAMPLE

4.1 Normal modes of a two-layer viscoelastic model

We define a simple reference spherically symmetric model $\mathbf{m}_0$. It consists of a 30-km thick homogeneous elastic lithosphere underlain by a homogeneous viscoelastic sphere with a Maxwell rheology. It is an analogue for a strong-crust underlain by a weak mantle suggested by many studies (e.g. Kaufmann & Amelung 2000; Pollitz *et al.* 2001; Nishimura & Thatcher 2003). We assign elastic parameters $\lambda = \mu = 30$ GPa and a sublithosphere viscosity of $\eta = 10^{19}$ Pa s. On a viscoelastic structure with a finite number of layers there are, for every spherical harmonic degree, a finite number of viscoelastic modes but an infinite number of static modes. A dispersion diagram of the viscoelastic models (Fig. 2) shows the three dispersion branches for spheroidal modes and one dispersion branch for toroidal modes present on the two-layer model. Fig. 3 shows the corresponding radial functions U, V and W associated with degree $l = 2000$. In such a two-layer model, mode energy is always concentrated near the base of the elastic layer. This implies that deeper sources (in the elastic layer) stimulate a larger post-seismic response
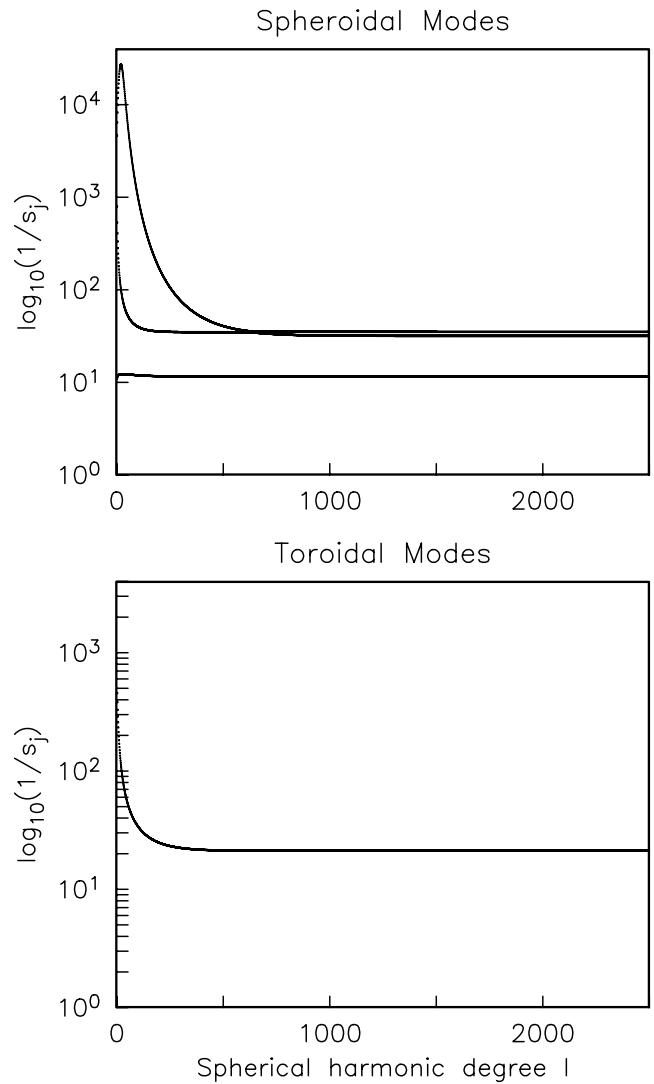

Figure 2. Dispersion diagram of inverse decay times s_j^{-1} versus spherical harmonic degree for an earth model with a 30 km thick elastic plate overlying a uniform viscoelastic sphere of viscosity 10^{19} Pa s. Elastic parameters are $\lambda = \mu = 30$ GPa.

and that the post-seismic deformation is largest at the base of the elastic layer and top of the asthenosphere. This is in accord with physical intuition since, for a given source, the largest coseismic strains realized in the asthenosphere occur at the top of the asthenosphere, and relaxation of coseismic strains in this region has greatest effect on its immediate vicinity.

In order to concentrate the static modes on the area where 3-D perturbations are intended to be applied, the lower boundary of the elastic structure is assigned a l-dependent depth equal to 2.5 horizontal wavelengths below the depth of the perturbed volume, which is 96 km. For a spherical harmonic degree of $l = 2000$, the horizontal wavelength is 20 km; hence the free oscillations are computed for a spherical volume bounded by the free surface and a spherical shell at depth 146 km; traction-free boundary conditions are assigned at each boundary. Parts a–c of Supplementary Figs S-1 to S-4 show the radial functions of the free oscillations (static modes) of the 20 highest-frequency modes for $l = 2000$. At this l, the set of static modes captures static deformation at a minimum vertical wavelength of ~40 km.
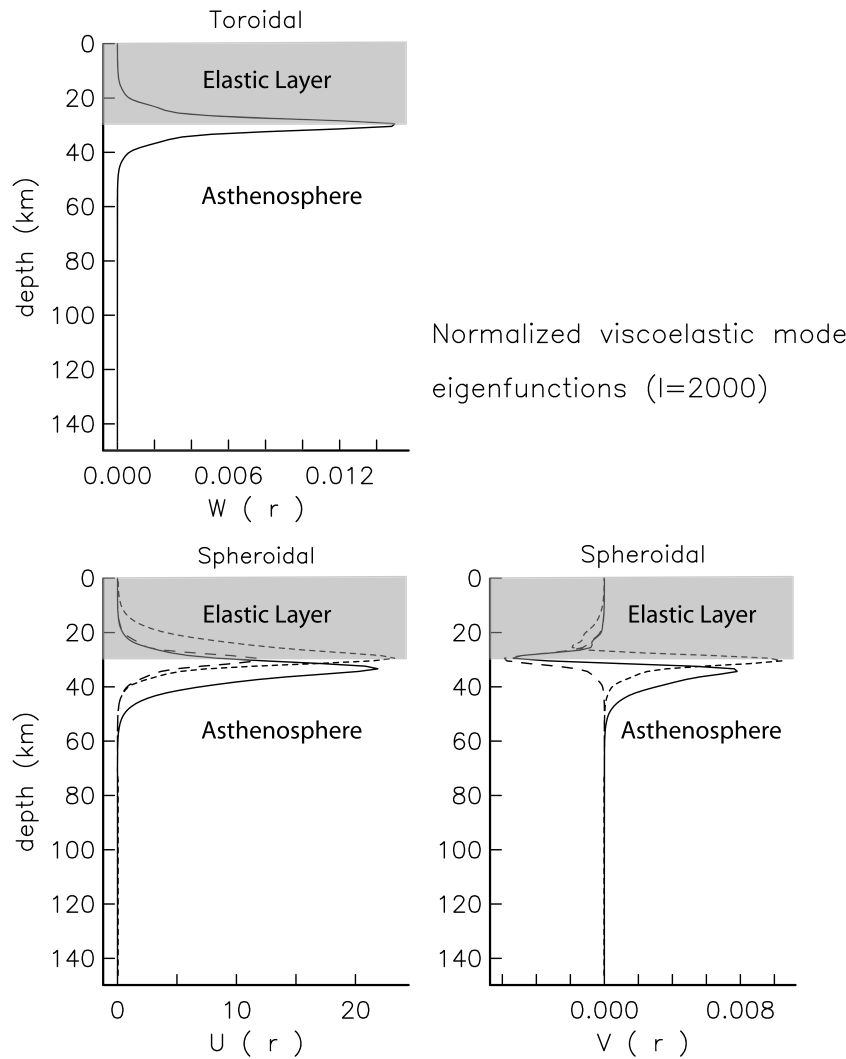
Figure 3. Radial functions $U(r)$, $V(r)$, and $W(r)$ associated with viscoelastic modes of degree $l = 2000$ on the two-layer viscoelastic structure.

Although individual static modes are non-local (i.e. distributed with similar amplitude at all depths), when weighted by the source excitation functions the deformation associated with the static modes is local in nature (i.e. concentrated at the source depth). This is in contrast with the viscoelastic modes (Fig. 3) which have localized radial functions but nevertheless have non-local effects (e.g. even shallow source can produce a substantial viscoelsatic response at all depths). This difference arises from the fact that, for a given l, there are a finite number of viscoelastic modes but an infinite number of static modes. The contrasting behaviour between static modes and viscoelastic modes can also be rationalized in terms of the asymptotic fall-off of displacement with distance from the source. For example, for an infinitely long vertical strike-slip fault with a finite width, the coseismic displacement field depends on distance from the fault r as $\sim r^{-1}$ but the post-seismic displacement field behaves as $\sim r^0$ after a sufficient elapsed time (Savage & Prescott 1978).

4.2 Post-thrusting relaxation with a slab structure

To the reference model $\mathbf{m}_0$ defined in the previous section we add a simple slab structure. Referring to Fig. 4, the aspherical perturbation is defined over an area Γ on the unit sphere of area 1.4×1.4 squared

geocentric degrees (5.97×10^{-4} rad^2). The slab structure dips 23°, is 32.6 km thick (30 km vertically) and extends from the base of the elastic lithosphere at 30 km depth to a lower depth of 96 km. Its viscosity is 3×10^{21} Pa s, that is, 300 times that of the surrounding sublithosphere. Its rigidity equals that of its surroundings. Its upper surface connects with the lower edge of a thrust-fault source dipping 15° in the elastic lithosphere.

For assigned dip slip of 5 m, the coseismic displacement field is synthesized using the Direct Greens Function (DGF) method of Pollitz (1996), truncated at $l_{max} = 2500$. For each spherical harmonic degree l, this method implements a point source on $\mathbf{m}_0$ in terms of a jump in the displacement-stress vector at the source radius; a finite source is implemented as a superposition of numerous point sources. From the normal mode perspective the resulting deformation field includes all static modes of a given l, of which there are infinitely many. Fig. 5 shows the coseismic displacement field calculated using the DGF method.

Post-seismic displacement fields are synthesized with eq. (2) on the spherically symmetric model $\mathbf{m}_0$ and with eq. (11) on the 3-D model $\mathbf{m}$. The calculation on $\mathbf{m}_0$ uses all viscoelastic modes, and the calculation on $\mathbf{m}$ uses all viscoelastic modes and the 22 highest static modes of the viscoelastic model truncated at $l_{max} = 2500$. Figs 6(a) and (b) show the post-seismic relaxation fields at times 10
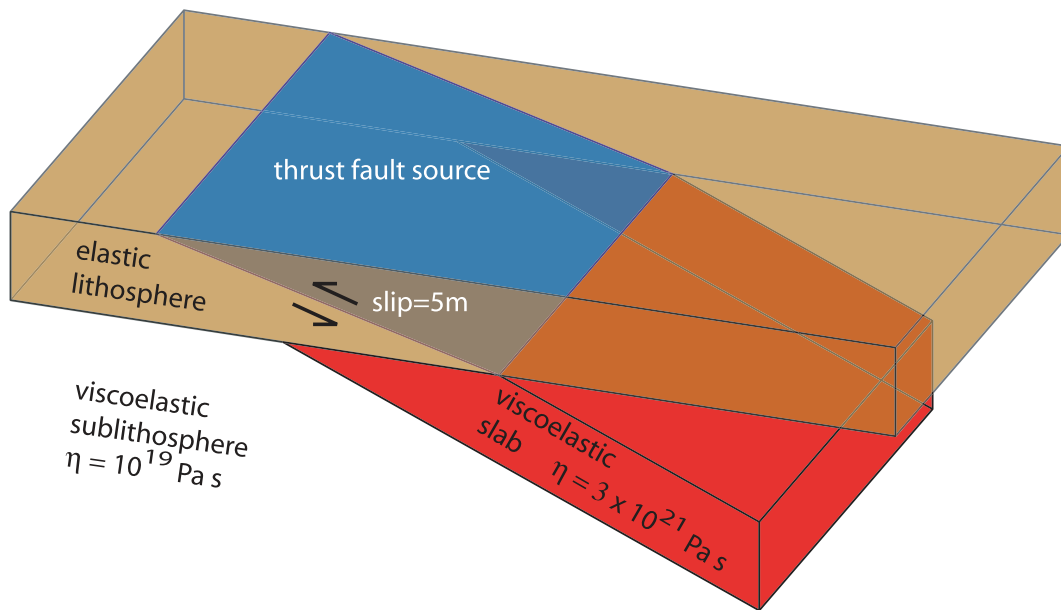
Figure 4. Geometry of post-thrusting relaxation in the presence of a slab structure. A thrust source dipping 15° ruptures the entire elastic lithosphere. It is connected at its base to the upper surface of a 23°-dipping, 32.6-km thick slab structure which extends to 96 km depth. The length of the thrust source as well as the slab structure is 1.4°, and the aspherical region Γ is that portion of the unit sphere occupied by slab structure, which has an area of 1.96 squared geocentric degrees.
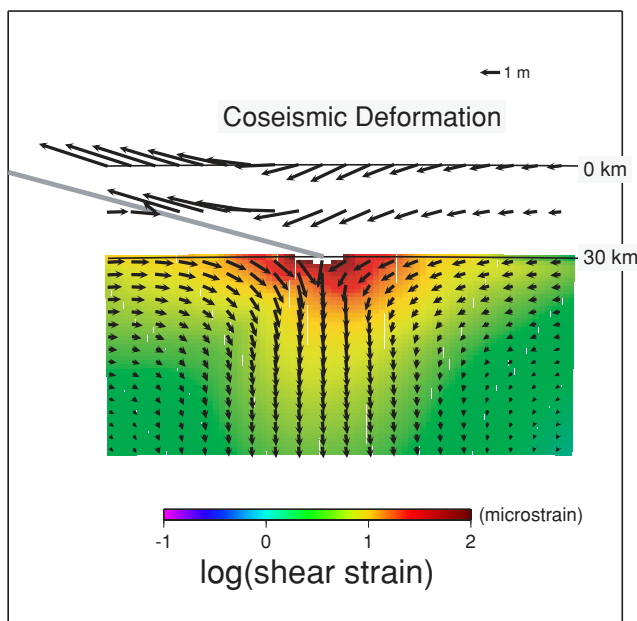

Figure 5. Coseismic displacement and strain fields from 5 m dip slip on a thrust fault (Fig. 4), using the DGF method (Pollitz 1996). The profile is on a vertical plane bisecting the fault.

and 25 yr after the synthetic event on $\mathbf{m}_0$ and $\mathbf{m}$, respectively. The shear strain shown in the figures refers to the maximum shear strain, which is equal to one-half the difference between the maximum and minimum principal strain. Comparing Figs 6(a) and (b), the effect of the slab is to amplify downdip displacements along the slab. This pattern is reasonable because the coseismic strain field has strong downdip contraction in the slab region just below the deeper extension of the fault. At times that are long compared with the Maxwell

relaxation time of the background medium ($\tau_{Max} = \eta/\mu = 10.6$ yr) but short compared with the Maxwell relaxation time of the slab ($300 \times \tau_{Max}$), we would expect the post-seismic deformation field to be a rigid downdip motion of the slab in an amount comparable with the coseismic displacement of the footwall of the thrust fault. That is, as the surrounding material relaxes, the slab would act approximately as a stress guide that would accommodate the motion imposed by the footwall of the fault.

5 POST-SEISMIC RELAXATION FOLLOWING THE 2004 SUMATRA EARTHQUAKE

The 2004 $M = 9.2$ Sumatra earthquake ruptured a ~1400 km long section of the Sunda and Sumatra trenches (Fig. 7) with up to 20 m of slip (Banerjee *et al.* 2007; Chlieh *et al.* 2007). Large coseismic stress displacements in the crust and upper mantle around the east Indian Ocean and southeast Asia regions resulted from the earthquake (Banerjee *et al.* 2005, 2007). Large post-seismic displacements are observed at Earth's surface (with GPS) for the first several months after the earthquake (Pollitz *et al.* 2006a). Viscoelastic models explored by Pollitz *et al.* (2006a) suggest similarly large post-seismic motions at depths up to several hundred kilometres below the surface. Fig. 8 shows observed time-series at four continuous GPS sites Banerjee *et al.* (2006) and the predictions of the Pollitz *et al.* (2006a) viscoelastic model. Both the December 2004 and March 2005 deformation sources (both co and post-seismic motions) are included in the modelled time-series. Even though this model was derived using only the first ~4 months post-seismic motions, it predicts well the surface post-seismic motions out to at least 1.25 yr after the earthquake. The details of the post-seismic flow fields generated at both the surface and at depth are sensitive to the rheology structure, which is assumed spherically symmetric in Pollitz *et al.* (2006a).
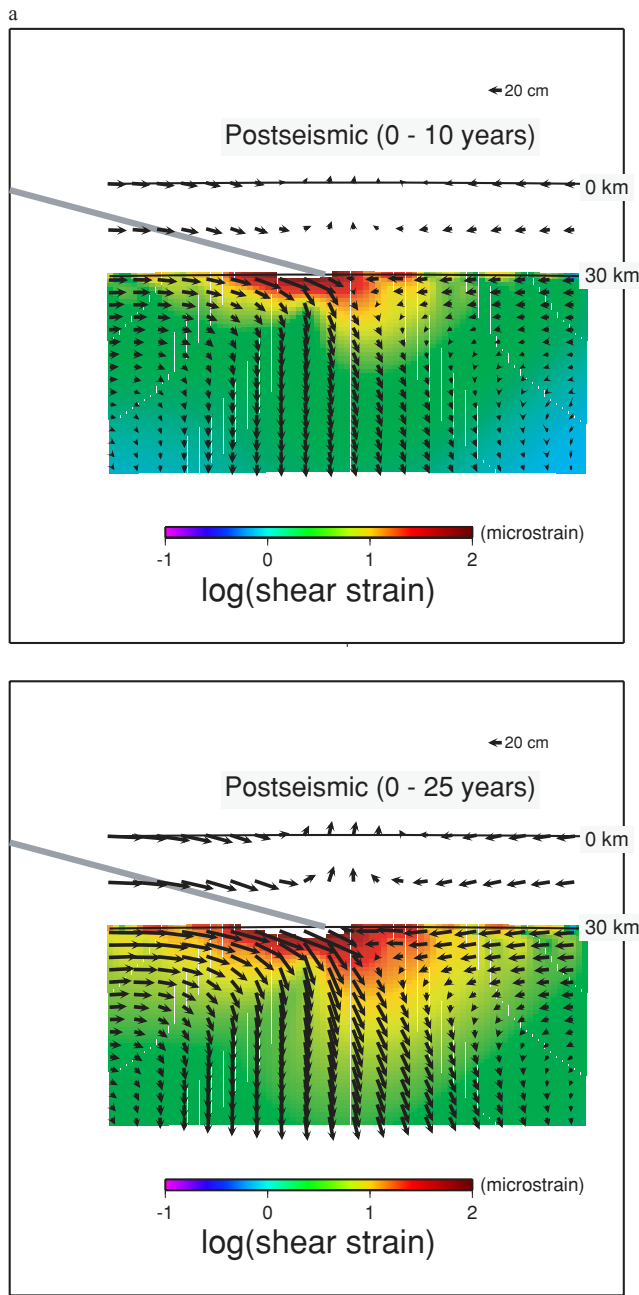
a

b

Figure 6. Post-seismic displacement and strain fields from 5 dip-slip on a thrust fault (Fig. 4), using all viscoelastic modes of the two-layer viscoelastic model $\mathbf{m}_0$ (Section 4.1). The profiles are on a vertical plane bisecting the fault. (a) Post-seismic deformation field on $\mathbf{m}_0$. (b) Post-seismic displacement and strain fields on $\mathbf{m}$, calculated with eq. (11) using all viscoelastic modes and the 22 highest static modes of the two-layer viscoelastic model $\mathbf{m}_0$. Shaded grey area delineates the slab.

We explore here how these flow fields are affected by the presence of a subducted slab structure extending deep into the mantle.

For laterally heterogeneous models we define the spherically symmetric rheology $\mathbf{m}_0$ to be the Burgers body rheology (Fig. 9) derived by Pollitz *et al.* (2006a) on the basis of fitting the first 6 months of regional post-seismic GPS time-series. The quasi-static deformation fields are synthesized with a spherical harmonic expansion out to a maximum degree of 800. We use the 22 lowest-frequency free oscillation modes per spherical harmonic degree to represent the
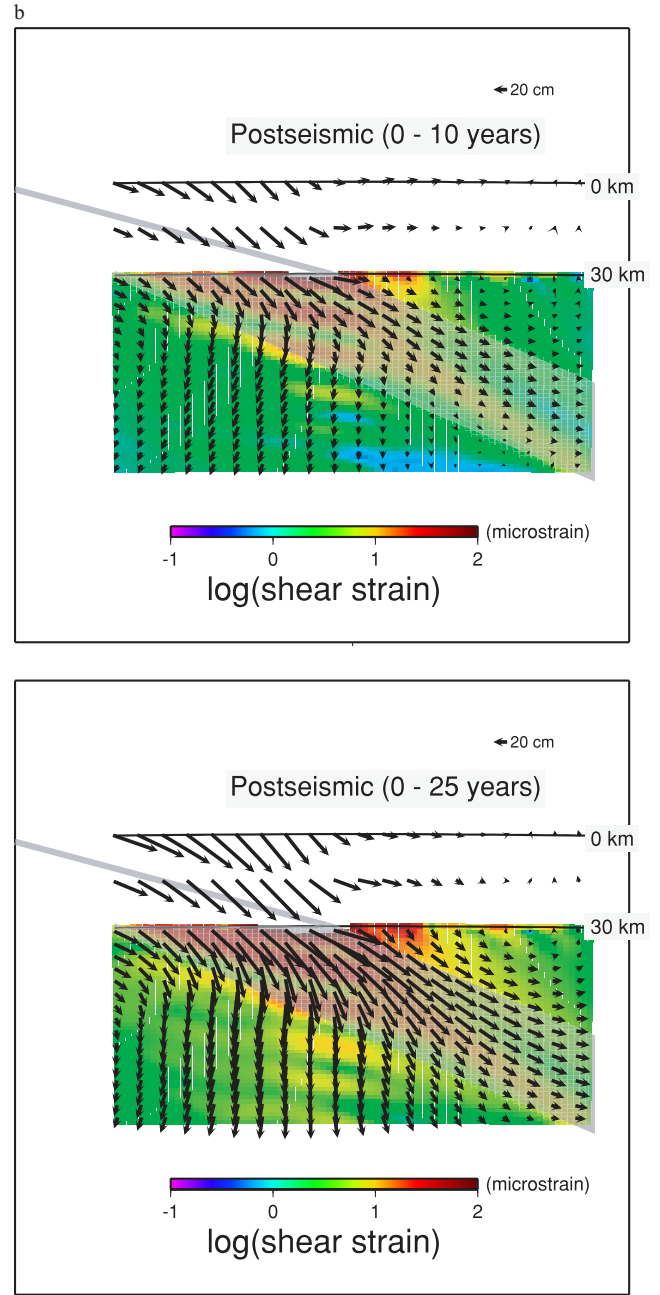
Figure 6. (*Continued.*)

static modes S^{static}. The viscoelastic modes S^{VE} consist of 6 toroidal and 17 spheroidal modes per spherical harmonic degree. The combined S^{static} and S^{VE} sample well the upper 300 km of the Earth and practically represent quasi-static deformation on $\mathbf{m}_0$ with a vertical resolution of $\sim$15 km and lateral resolution of $\sim$50 km.

5.1 Slab model

The slab structure is constrained by the depth contours of Gudmundsson & Sambridge (1998), which prescribe the depth to the top of the slab (Fig. 10, left-hand side). In order to evaluate the integral in eq. (13) it is necessary to discretize the slab on the unit sphere. Fig. 10 (right-hand side) shows the interpolated depth to the top of the slab at a lateral resolution of 13 km. The slab is assumed to
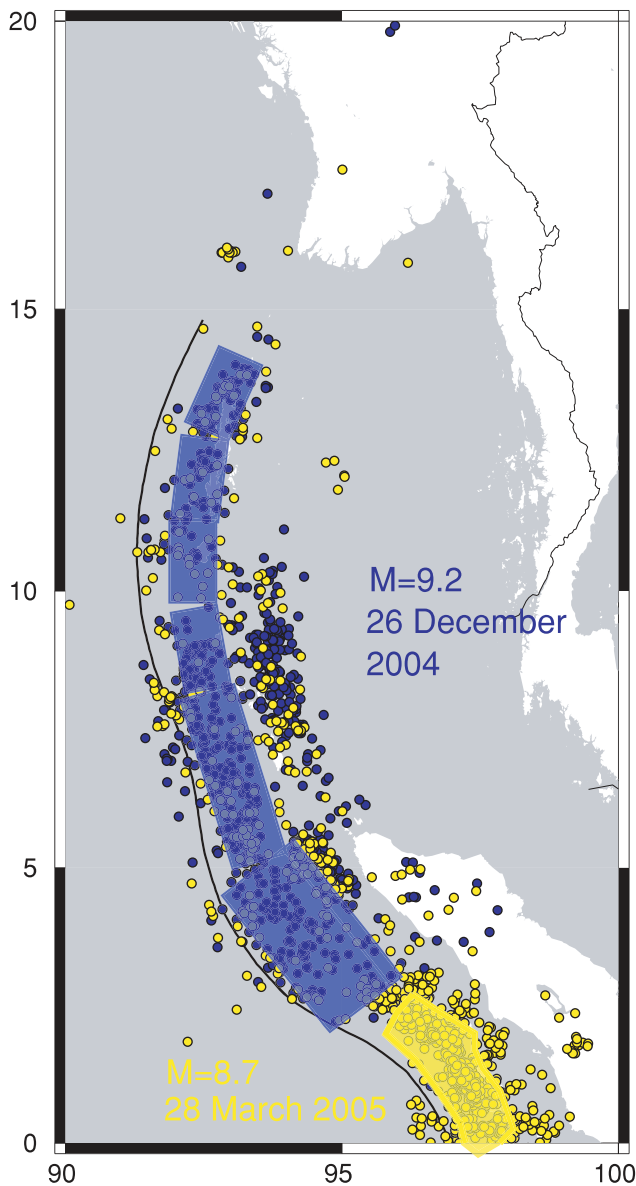
Figure 7. Rupture areas associated with the 2004 $M = 9.2$ Sumatra–Andaman and 2005 $M = 8.7$ Nias earthquakes. Blue planes are the coseismic rupture planes of the 2004 December 26 earthquake (Banerjee *et al.* 2007). Epicentres of $M \geq 4.0$ earthquakes from 2005 March 29 to 2005 August 1 from the NEIC catalogue are superimposed.

be 30 km thick. Where information of slab depth is lacking (e.g. the 250 km depth contour extends only up to 11°N), the slab is truncated at depth. Fig. 11 shows a 3-D view of the slab with the locations of major vertical discontinuities in the viscoelastic structure. It shows that slab material is present along almost the entire lateral extent of the 2004 Sumatra rupture down to the base of the asthenosphere.

Fig. 12 shows the coseismic motions of the 2004 Sumatra earthquake, calculated using the DGF method, in a SW–NE depth section. As in Section 4.2, post-seismic displacement fields are synthesized with eq. (2) on $\mathbf{m}_0$ and with eq. (11) on the 3-D model $\mathbf{m}$. The calculation on $\mathbf{m}_0$ uses all viscoelastic modes, and the calculation on $\mathbf{m}$ uses all viscoelastic modes and the 22 highest static modes of the viscoelastic model truncated at $l_{max} = 800$. Fig. 13 shows the cumulative post-seismic relaxation field of the 2004 Sumatra earthquake 1 yr after the event on both $\mathbf{m}_0$ and $\mathbf{m}$. The post-seismic motions with

the slab (Fig. 13, bottom) are more vigorous in the near-field region (within ∼100 km of the slab) but reduced on the flanks, compared with the motions predicted without the slab (Fig. 13, top). Particularly on the continental side, the horizontal post-seismic flow field directly above the slab is substantially reduced, and the vertical near-surface motions more pronounced. The patterns at Earth's surface are seen more clearly in Figs 14(a) and (b). (Both Figs 13 and 14 do not include the coseismic motions from the 2005 Nias earthquake.) Overall, the horizontal and vertical displacements in the far field on the continental side are reduced about 20 per cent because of the effect of the slab. As a result, predicted post-seismic motions at far-field GPS sites are too small when the slab is included and rheological parameters estimated from a spherical model are used (dashed lines in Fig. 8).

5.2 Effects of mantle wedge and elastic plate thickness

Several factors could offset the damping effects of the slab in the far field. This includes a reduction in elastic plate thickness or a reduction in asthenosphere viscosity in the mantle wedge on the continental side. Both effects were considered by Hu *et al.* (2004) in their study of the 1960 Chile earthquake post-seismic deformation. Here we consider viscoelastic structures which include a relatively low viscosity mantle wedge. As in Section 5.1 we define the spherically symmetric model $\mathbf{m}_0$ to be the Burgers body rheology of Pollitz *et al.* (2006a) with steady state asthenosphere viscosity $\eta^{(1)} = 10^{19}$ Pa s and transient asthenosphere viscosity $\eta^{(2)} = 5 \times 10^{17}$ Pa s. Superimposed on $\mathbf{m}_0$ is a combination of the slab structure (Fig. 11) and a mantle wedge with Burgers body rheology and associated viscosities that are 40 per cent those of the surrounding asthenosphere. This mantle wedge is restricted to the volume lying above those portions of the slab with slab depth not exceeding 150 km. The first-year post-seismic surface deformation field (without 2005 Nias coseismic motions) is shown in Fig. 14(c). Comparison of Figs 14(b) and (c) shows that the low-viscosity mantle wedge substantially modifies the near-field post-seismic vertical response, up to ∼15 per cent primarily in the area close to the lower fault edges, with little change in the far-field horizontal or vertical response. As with the slab-only model, the far-field horizontal GPS time-series are underpredicted by this model. For example, predicted first-year post-seismic motions at PHKT are about 10 cm without Nias coseismic motions (e.g. Fig. 14b) and 14 cm with Nias coseismic motions, somewhat less than the 21 cm post-seismic vector motion observed during the first year (Fig. 8). We find that reducing the viscosity of the mantle wedge still further does not substantially increase the first-year post-seismic displacements any further, since the volume with very low viscosity achieves near complete relaxation within the first year.

In order to counteract the damping effect of the slab and increase the modelled far-field post-seismic displacements, we decrease elastic plate thickness from $H = 62$ to 50 km. The resulting displacement field (Fig. 14d) is about 8 per cent larger in the far field. However, as with the other laterally heterogeneous viscoelastic models, the predicted first-year far-field horizontal displacements remain smaller than observed far-field displacements. The most effective way to counteract the slab effect in the far-field would be to reduce the average asthenosphere viscosity values. Constraining the asthenosphere viscosities in this fashion depends further on the dependence of post-seismic motions on the joint processes of asthenosphere relaxation and fault afterslip. In the following section we consider these processes in the context of the asthenosphere viscosities estimated on the laterally homogeneous model.
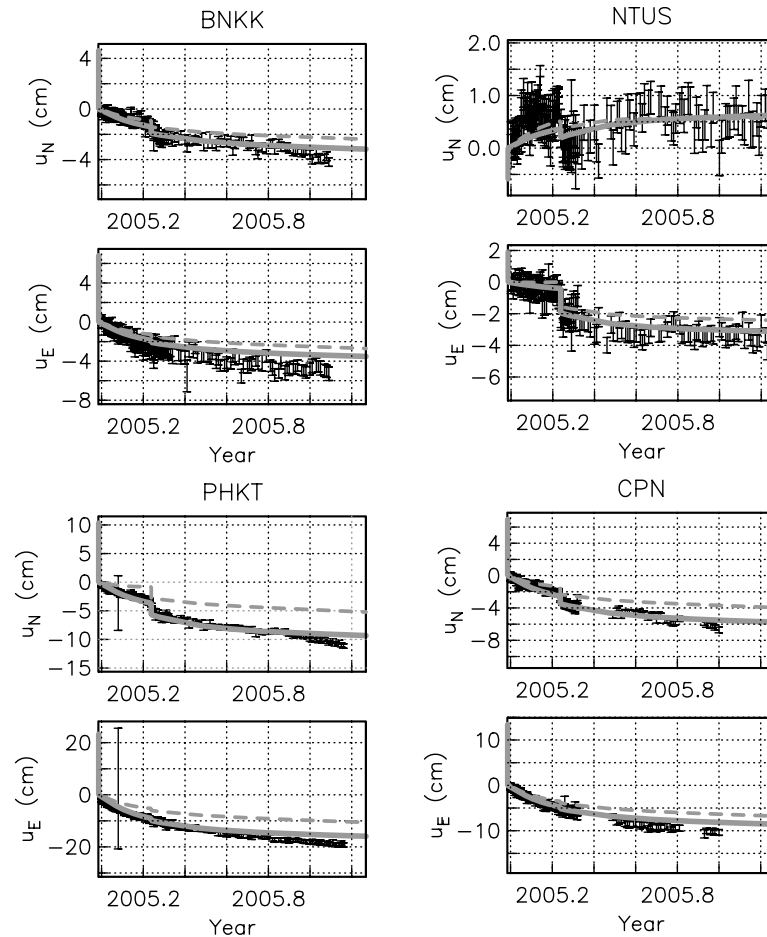
Figure 8. Horizontal post-seismic time-series at four sites (Banerjee *et al.* 2006) (locations in Fig. 15). These time-series have been corrected for background interseismic motions (Apel *et al.* 2006). Superimposed are the predictions of the Pollitz *et al.* (2006a) viscoelastic model (Fig. 9) without the slab (solid grey curves) and with the slab (dashed grey curves). The model time-series include the effects of coseismic and post-seismic motions generated by both the 2004 December and 2005 March events.
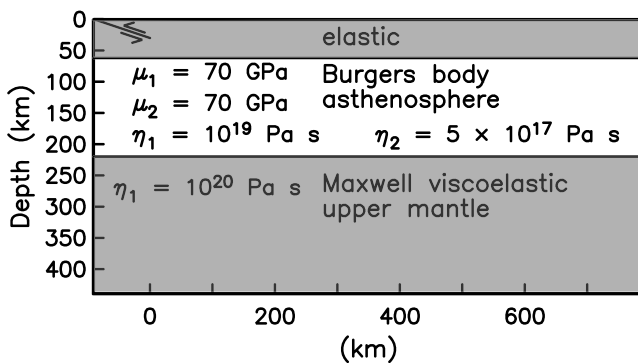

Figure 9. Spherically symmetric viscoelastic structure derived by Pollitz *et al.* (2006a). The asthenosphere at depth from 62 to 220 km has a Burgers body rheology with indicated parameters, and the underlying mantle is assumed Maxwell viscoelastic with the indicated viscosity.

6 GPS DATA SET

We have compiled data from sites belong to various continuously operating GPS (CGPS) networks and several sites surveyed in campaign-mode (SGPS) before and after the event by the Survey of India (SOI) (Gahalaut *et al.* 2006; Pollitz *et al.* 2006b; Banerjee *et al.* 2007). GPS data from the CGPS sites were processed with the

GAMIT/GLOBK software package (King & Bock 2005; Herring 2005) to produce time-series of station coordinates in the ITRF-2000 reference frame. We used 18 global IGS GPS stations to implement the ITRF-2000 reference frame in the GPS analysis. Stations used to define the reference frame are >4500 km from the earthquake rupture. The observations were compiled to yield a 3-D displacement field spanning the time interval 2005 January–November (Fig. 15 and Table 1). All contributing networks were operational at the time of the 2004 December earthquake or within 30 d thereafter. The 11-month displacement field given in Table 1 is obtained after removal of March 2005 Nias coseismic offsets as well as interseismic displacements estimated from a regional relative plate motion model (Apel *et al.* 2006).

7 DISCUSSION

Among the laterally heterogeneous models considered in section 5, the model of combined slab, mantle wedge and reduced elastic plate thickness ($H = 50$ km) compares best with the observations. We use it to predict the first-11 months horizontal and vertical motions described in Section 6. In Fig. 15 these are compared with observed post-seismic motions. There is good agreement in the horizontal and vertical motions at far-field sites (CPN, BNKK, CHMI and PHKT) and fair agreement in the near-field horizontal motions around the
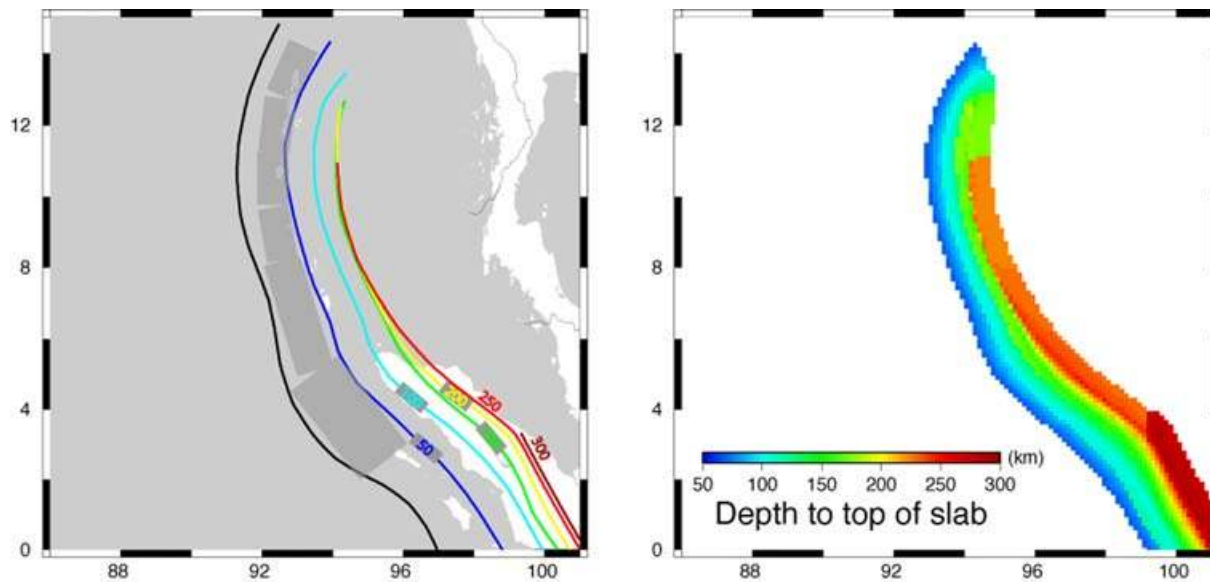
Figure 10. Left-hand side: Depth to the top of the slab as prescribed by Gudmundsson & Sambridge (1998). The trench axis is indicated with the black contour (Curray 2005), and rupture planes of the 2004 Sumatra earthquake indicated with grey planes (Banerjee *et al.* 2007). Right-hand side: The slab contours are interpolated on a fine grid of points $\hat{\mathbf{r}}'$ used to evaluate the integral in eq. (13).
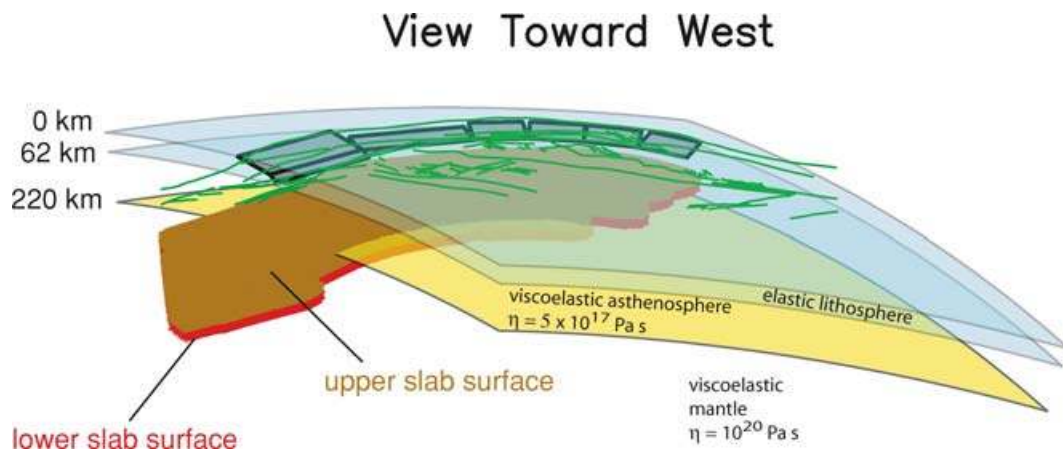

Figure 11. 3-D view of slab structure towards the west. Major vertical discontinuities in the viscoelastic structure include the free surface, the base of the elastic plate (62 km), and the base of the asthenosphere (220 km). Surface faults are indicated with green lines (Curray 2005). Rupture planes of the 2004 Sumatra earthquake indicated with grey planes (Banerjee *et al.* 2007).

southern half of the 2004 Sumatra rupture (UMLH, CAMP and KARD), where model and observed horizontal motions are coherent but misfits are several times the standard deviations of the observed motions. Neither the horizontal nor the vertical component displacements are adequately predicted in the near field around the Andaman Islands north of 8°N or around the Nias rupture zone; in both regions model and observed horizontal motions are not correlated or seriously anticorrelated. (Note that observations at SUGAR sites generally did not begin until 30 d after the 2004 Sumatra earthquake. With the exception of UMLH their predicted post-seismic motions are dominated by viscoelastic relaxation following the 2005 Nias earthquake.) On the other hand, vertical displacements at the Andaman sites are systematically better predicted on the laterally heterogeneous viscoelastic model than on the laterally homogeneous model (Fig. 15b).

Remaining discrepancies between observed and predicted displacements may be explained with a combination of the following:

(1) Afterslip along the coseismic rupture plane and/or its downdip extension. (2) Viscoelastic relaxation with other prescriptions of lateral heterogeneity. (3) Use of a different coseismic fault geometry (2004 earthquake) than has been hitherto assumed, or (4) Poroelastic rebound. The first explanation is supported by the large discrepancies in both horizontal and vertical motions south of ∼2°N as recorded by the SUGAR network; these discrepancies may be well explained with predominantly afterslip updip of the 2005 Nias coseismic rupture (Briggs *et al.* 2006; Hashimoto *et al.* 2006; Hsu *et al.* 2006). Substantial afterslip following the Nias earthquake is further supported by the relatively small post-seismic motion predicted by the viscoelastic model at SAMP (Fig. 15a), a CGPS site which was recording continuously through both the 2004 Sumatra and 2005 Nias events. In the Andaman Islands, afterslip downdip of the coseismic rupture could plausibly produce both the post-seismic uplifts (Fig. 15b) and westward motions (Fig. 15a) of Andaman sites. This explanation is supported by the westward post-seismic
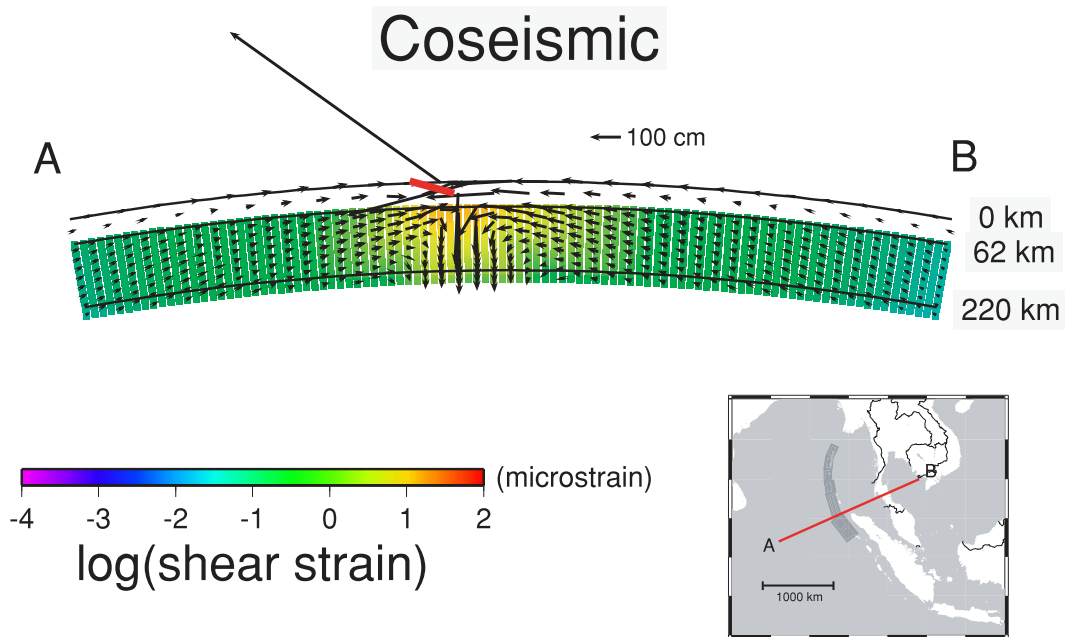
Figure 12. Vector coseismic displacement field resolved along the vertical profile indicated in the inset. The shear strain value is one-half the difference between the maximum and minimum principal strains. The red line segment is the trace of the Sumatra rupture at the profile location.
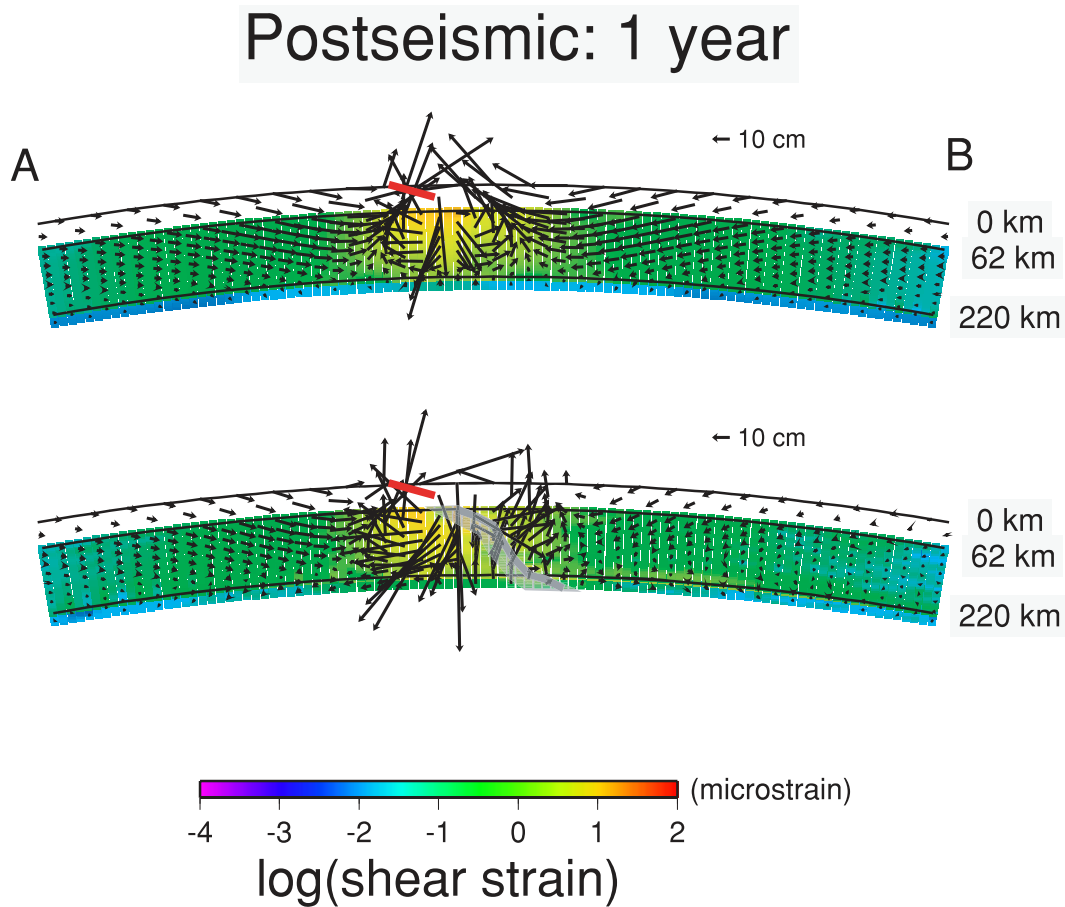

Figure 13. Cumulative post-seismic displacement and strain fields from the 2004 Sumatra earthquake evaluated one year after the event. (top) Post-seismic deformation field on $\mathbf{m}_0$ (without slab). Profile location shown in inset of Fig. 12. (bottom) Post-seismic displacement and strain fields on $\mathbf{m}$ (with slab), calculated with eq. (11) using all viscoelastic modes and the 22 highest static modes of the viscoelastic model $\mathbf{m}_0$. Shaded grey area delineates the slab.
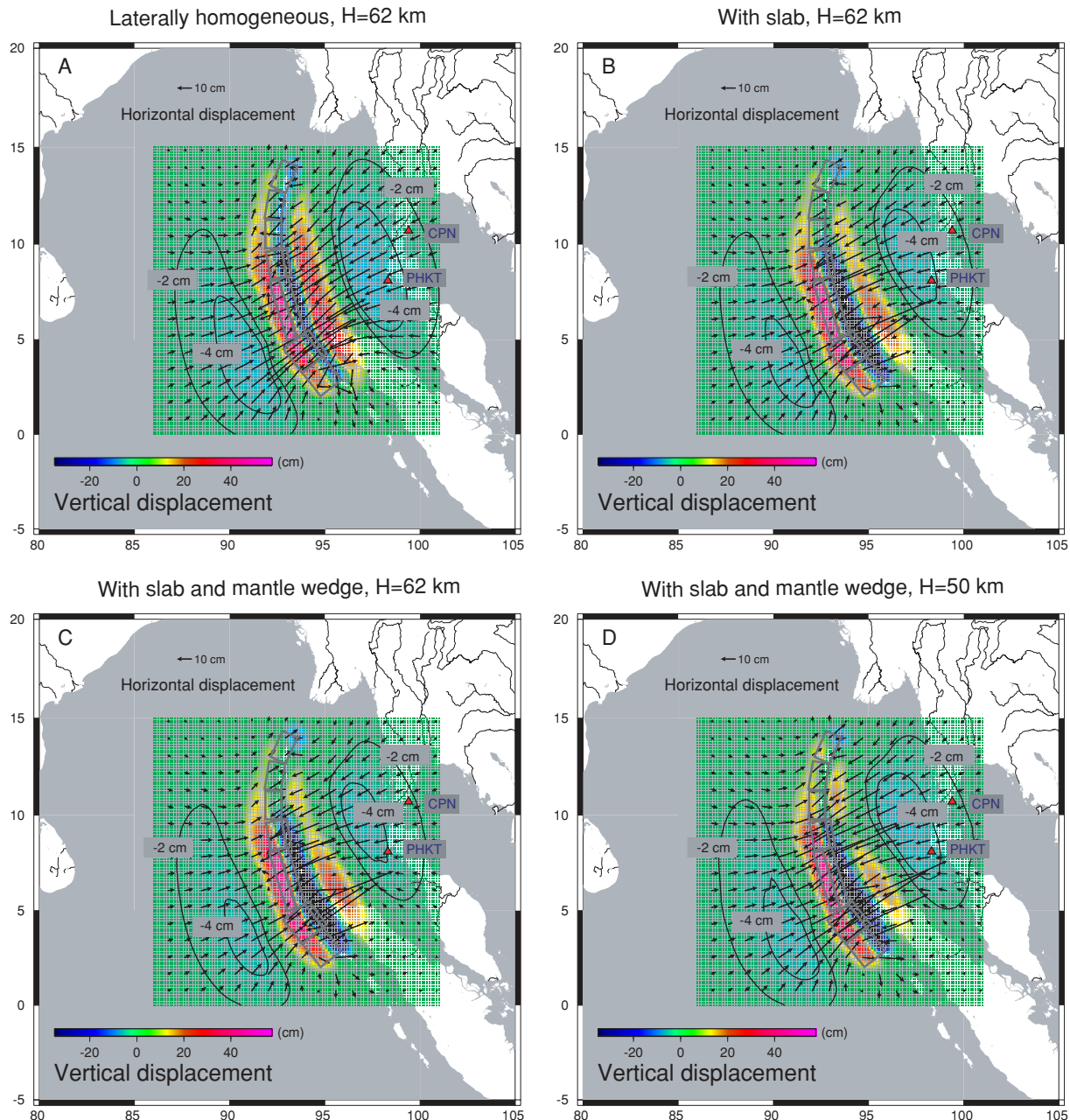
Postseismic Displacement Field (t=1 year)

Laterally homogeneous, H=62 km

With slab, H=62 km

With slab and mantle wedge, H=62 km

With slab and mantle wedge, H=50 km

Figure 14. First-year post-seismic displacement field at the surface from the 2004 Sumatra earthquake: (a) Laterally homogeneous, without slab, elastic plate thickness $H = 62$ km. (b) Laterally heterogeneous, with slab, $H = 62$ km. (c) Laterally heterogeneous, with slab and mantle wedge, $H = 63$ km. (d) Laterally heterogeneous, with slab and mantle wedge, $H = 50$ km. In all plots, contours for the vertical displacement field are superimposed.

motions at PHKT and CPN (Fig. 15a), which are ~40 per cent too small using viscoelastic relaxation alone and which would be amplified by post-seismic afterslip. It is further supported by a composite PORT/CAR2 time-series beginning 25 d after the Sumatra earthquake (fig. 7 of Banerjee *et al.* 2007), which shows post-seismic uplift in Port Blair has occurred continuously since that time. Alternatively, inclusion of the slab structure and weak mantle wedge each promote post-seismic uplift of Andaman sites. These effects could be amplified by prescription of a weaker mantle wedge in this area. The third possibility is a revision in the location of the

coseismic rupture planes prescribed along the megathrust north of ~8°N. The precise location of the interplate boundary is uncertain (Banerjee *et al.* 2007), and even a small eastward shift in the locations of the boundary would produce the observed post-seismic uplift of these sites. However, the same shift would produce strong eastward post-seismic motions, contrary to observation (Fig. 15a). Among the above explanations, a combination of afterslip following the 2004 Sumatra earthquake around the Andaman Islands and a weaker mantle wedge—in addition to relaxation of a low-viscosity asthenosphere—appear most likely.
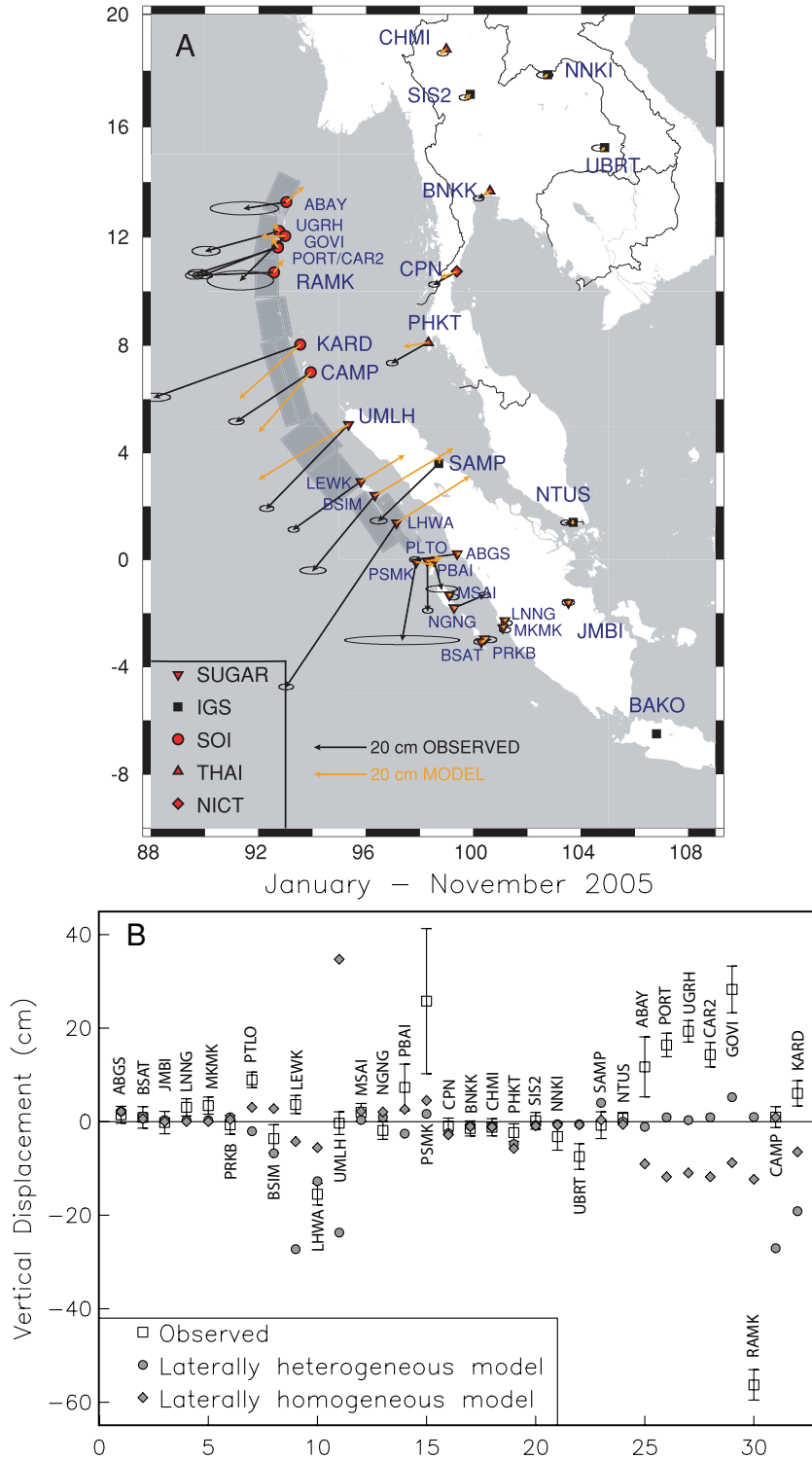
Figure 15. Horizontal (a) and vertical (b) post-seismic displacements with 1σ errors at GPS sites from the combined 2004 Sumatra and 2005 Nias earthquakes, evaluated for the first 11 months following the 2004 earthquake. Model displacement vectors are on the laterally heterogeneous model with slab and mantle wedge and elastic plate thickness $H = 50$ km. They include only viscoelastic relaxation and no Nias coseismic offsets. Observed displacements during 2005 January–November (Table 1) are with 2005 Nias coseismic offsets and interseismic motions removed.

Table 1. CGPS and SGPS measured horizontal surface displacements from 2005 January to November and their 1σ uncertainties.

$Lat.^\circ N$	Lon. $^\circ$E	E_{offset} cm	N_{offset} cm	Up_{offset} cm	E_{sig} cm	N_{sig} cm	Up_{sig} cm	Site
0.221	99.388	−16.51	−2.24	1.47	0.87	0.44	1.81	ABGS
−3.077	100.285	−0.31	0.14	0.92	1.07	0.47	2.30	BSAT
−1.615	103.520	−0.01	0.17	−0.19	0.98	0.51	2.38	JMBI
−2.285	101.156	0.73	−0.90	3.06	0.91	0.45	1.85	LNNG
−2.543	101.091	0.84	−0.87	3.44	0.90	0.45	1.83	MKMK
−2.967	100.400	2.44	−0.26	−0.67	0.98	0.46	2.02	PRKB
−0.055	98.280	0.13	−19.21	8.95	0.83	0.43	1.66	PTLO
2.409	96.326	−24.16	−29.26	−3.63	2.08	0.58	3.00	BSIM
2.923	95.804	−26.23	−18.64	3.67	0.90	0.43	1.93	LEWK
1.383	97.134	−43.09	−63.96	−15.51	1.18	0.46	2.32	LHWA
5.053	95.339	−31.82	−32.68	−0.32	1.12	0.48	2.43	UMLH
−1.326	99.089	1.51	−0.76	2.02	0.89	0.45	1.88	MSAI
−1.800	99.268	11.98	5.01	−1.89	0.91	0.45	1.90	NGNG
−0.032	98.526	2.98	−11.02	7.33	2.51	0.53	4.97	PBAI
−0.089	97.861	−5.48	−30.43	25.77	9.16	0.70	15.52	PSMK
10.725	99.374	−8.87	−4.99	−1.00	0.87	0.42	1.77	CPN
13.668	100.607	−4.45	−2.77	−1.46	0.83	0.43	1.61	BNKK
18.771	98.973	−1.26	−1.54	−1.20	0.89	0.45	1.83	CHMI
8.105	98.308	−14.07	−7.97	−2.34	0.93	0.44	1.88	PHKT
17.157	99.867	−2.13	−1.20	0.18	0.88	0.44	1.79	SIS2
17.865	102.747	−1.05	−0.14	−3.19	1.29	0.52	2.90	NNKI
15.245	104.871	−1.94	−0.12	−7.44	1.26	0.51	2.74	UBRT
3.622	98.715	−23.57	−22.55	−0.75	1.35	0.52	2.85	SAMP
1.346	103.680	−2.82	0.47	0.74	0.72	0.41	1.23	NTUS
13.278	93.028	−16.34	−2.51	11.71	5.45	1.04	6.41	ABAY
11.649	92.721	−29.42	−11.30	16.40	1.58	0.55	2.52	PORT
12.217	92.773	−28.63	−7.80	19.32	2.24	0.73	2.30	UGRH
11.614	92.720	−31.14	−9.94	14.32	1.60	0.55	2.61	CAR2
12.036	92.984	−17.43	−17.32	28.27	5.29	1.53	5.00	GOVI
10.697	92.570	−30.95	−1.17	−56.28	1.46	0.61	3.26	RAMK
7.005	93.934	−28.96	−19.23	0.98	1.23	0.50	2.24	CAMP
8.036	93.549	−56.88	−20.61	6.05	2.56	0.66	2.70	KARD

A remaining possibility is rebound of the crust driven by poroelastic flow in the crust and/or mantle. This process is responsible for short-wavelength post-earthquake vertical motions in Iceland from the 2000 June South Iceland Seismic Zone earthquakes (Jónsson *et al.* 2003) and possibly in California from the 1992 Landers earthquake (Fialko 2004). It is a candidate process for stress interaction between the 2004 Sumatra and 2005 Nias events (Masterlark 2006). This process deserves further exploration for its possible impact on long-wavelength post-earthquake deformation.

8 CONCLUSIONS

We have considered small-scale and large-scale examples of post-thrusting relaxation on viscoelastic structures that include a relatively high-viscosity slab embedded in a low-viscosity asthenosphere. Both the subsurface and surface post-seismic flow patterns are strongly affected by the presence of the slab structure relative to a slabless viscoelastic structure. Application to the 2004 Sumatra and 2005 Nias earthquakes demonstrates that viscoelastic relaxation governed by a low-viscosity asthenosphere with Burgers body rheology explains most of the horizontal and vertical post-seismic motions in the far field during the first year after the 2004 Sumatra earthquake. However, substantial discrepancies between predicted viscoelastic-model and observed near-field motions around the Andaman Islands, as well as around the Nias rupture zone, support the process of afterslip having occurred in these regions at least during the first post-seismic year.

REFERENCES

Apel, E.V., Bürgmann, R., Banerjee, P. & Nagarajan, B., 2006. Geodetically constrained Indian Plate motion and implications for plate boundary deformation, *EOS, Trans. Am. geophys. Un.,* **87**(52), T51B–1524.

Banerjee, P., Pollitz, F.F. & Bürgmann, R., 2005. Size and duration of the great 2004 Sumatra-Andaman earthquake from far-field static offsets, *Science,* **308,** 1769–1772.

Banerjee, P., Pollitz, F.F., Bürgmann, R. & Grijalva, K., 2006. Post-seismic deformation following the great 2004 Sumatra-Andaman and 2005 Nias earthquakes from GPS data, *EOS, Trans. Am. geophys. Un.,* **87**(52), G31A–01.

Banerjee, P., Pollitz, F.F. & Bürgmann, R., 2007. Coseismic slip distributions of the 26 December 2004 Sumatra-Andaman and 28 March 2005 Nias earthquakes from GPS static offsets, *Bull. seism. Soc. Am.,* **97**(1a), S86–102.

Briggs, R.W. et al., 2006. Deformation and slip along the Sunda megathrust in the Great 2005 Nias-Simeulue earthquake, *Science,* **311**, 1897–1901.

Chlieh, M. et al., 2007. Coseismic slip and afterslip of the Great (Mw 9.15) Sumatra-Andaman earthquake of 2004, *Bull. seism. Soc. Am.,* **97**(1a), S152–173.

Cohen, S.C., 1996. Time-dependent uplift of the Kenai Peninsula and adjacent regions of south central Alaska since the 1964 Prince William Sound earthquake, *J. geophys. Res.,* **101**, 8595–8604.

Curray, J.R., 2005. Tectonics and history of the Andaman Sea region, *J. Asian Earth Sci.,* **25**, 187–232.

Dahlen, F., 1980. A uniformly valid asymptotic representation of normal multiplet spectra on a laterally heterogeneous Earth, *Geophys. J. R. astr. Soc.,* **62**, 225–247.

Du, Y., Segall, P. & Gao, H., 1994. Dislocations in inhomogeneous media via a moduli-perturbation approach: general formulation and 2-D solutions, *J. geophys. Res.,* **99**, 13 767–13 779.

Fialko, Y., 2004. Evidence of fluid-filled upper crust from observations of post-seismic deformation due to the 1992 Mw7.3 Landers earthquake, *J. geophys. Res.,* **109**, B08401.

Friederich, W., 1999. Propagation of seismic shear and surface waves in a laterally heterogeneous mantle by multiple forward scattering, *Geophys. J. Int.,* **136**, 180–204.

Friederich, W., 2003. The S-velocity structure of the east Asian mantle from inversion of shear and surface waveforms, *Geophys. J. Int.,* **153**, 88–102.

Gahalaut, V.K., Nagarajan, B., Catherine, J.K. & Kumar, S., 2006. Constraints on 2004 Sumatra-Andaman earthquake rupture from GPS measurements in Andaman-Nicobar Islands, *Earth planet. Sci. Lett.,* **242**, 365–374.

Gudmundsson, O. & Sambridge, M., 1998. A regionalized upper mantle (RUM) model, *J. geophys. Res.,* **103**, 7121–7136.

Hashimoto, M. et al., 2006. Postseismic deformations following the Sumatra-Andaman and Nias earthquakes detected by continuous GPS observation in SE Asia, *Seism. Res. Lett.,* **77**, 289.

Herring, T., 2005. GLOBK: Global Kalman Filter VLBI and GPS Analysis Program, v.10.2, *Mass. Inst. of Tech.*

Hsu, Y.-J. et al., 2006. Frictional afterslip following the 2005 Nias-Simeulue earthquake, Sumatra, *Science,* **312**, 1921–1926.

Hu, Y., Wang, K., He, J., Klotz, J. & Khazaradze, G., 2004. Three-dimensional viscoelastic finite element model for postseismic deformation of the great 1960 Chile earthquake, *J. geophys. Res.,* **109**, B12403.

Ivins, E., 1996. Transient creep of a composite lower crust 2. a polymineralic basis for rapidly evolving postseismic deformations modes, *J. geophys. Res.,* **101**, 28 005–28 028.

Jónsson, S., Segall, P., Pedersen, R. & Björnsson, G.B., 2003. Post-earthquake ground movements correlated to pore-pressure transients, *Nature,* **424**, 179–183.

Kaufmann, G. & Amelung, F., 2000. Reservoir-induced deformation and continental rheology in the vicinity of Lake Mead, Nevada, *J. geophys. Res.,* **105**, 16 341–16 358.

King, R. & Bock, Y., 2005. Documentation for the GAMIT GPS Analysis software, release 10.2, *Mass. Inst. of Tech., Scripps Inst. Oceanogr.*

Masterlark, T., 2003. Finite element model predictions of static deformation from dislocation sources in a subduction zone: Sensitivities to homogeneous, isotropic, Poisson-solid, and half-space assumptions, *J. geophys. Res.,* **108**(B11), 2540, doi:10.1029/2002JB002296.

Masterlark, T., 2006. Poroelastic coupling of the recent M9 and M8.7 earthquakes in the Sumatra-Andaman subduction zone, *EOS, Trans. Am. geophys. Un.,* **86**(52), U11A–0802.

Meltzner, A., Sieh, K., Abrams, M., Agnew, D., Hudnut, K., Avouac, J.-P. & Natawidjaja, D., 2006. Uplift and subsidence associated with the Great Aceh-Andaman earthquake of 2004, *J. geophys. Res.,* **111**, B02407.

Nishimura, T. & Thatcher, W., 2003. Rheology of the lithosphere inferred from postseismic uplift following the 1959 hebgen lake earthquake, *J.*

geophys. Res., **108**, B82389.

Pollitz, F.F., 1996. Coseismic deformation from earthquake faulting on a layered spherical earth, *Geophys. J. Int.,* **125**, 1–14.

Pollitz, F.F., 1997. Gravitational viscoelastic postseismic relaxation on a layered spherical earth, *J. geophys. Res.,* **102**, 17 921–17 941.

Pollitz, F.F., 2003a. Postseismic relaxation theory on a laterally heterogeneous viscoelastic model, *Geophys. J. Int.,* **155**, 57–78.

Pollitz, F.F., 2003b. Transient rheology of the uppermost mantle beneath the Mojave Desert, California, *Earth planet. Sci. Lett.,* **215**, 89–104.

Pollitz, F.F., Wicks, C. & Thatcher, W., 2001. Mantle flow beneath a continental strike-slip fault: Postseismic deformation after the 1999 Hector Mine earthquake, *Science,* **293**, 1814–1818.

Pollitz, F.F., Banerjee, P. & Bürgmann, R., 2006a. Postseismic relaxation following the great 2004 Sumatra-Andaman earthquake on a compressible self-gravitating Earth, *Geophys. J. Int.,* **167**, 397–420.

Pollitz, F.F., Banerjee, P., Bürgmann, R., Hashimoto, M. & Choosakul, N., 2006b. Stress changes along the Sunda trench following the 26 December 2004 Sumatra-Andaman and 28 March 2005 Nias earthquakes, *Geophys. Res. Lett.,* **33**, L06309, doi:10.1029/2005GL02455.

Savage, J.C. & Prescott, W.H., 1978. Asthenospheric readjustment and the earthquake cycle, *J. geophys. Res.,* **83**, 3369–3376.

Yuen, D. & Peltier, W., 1982. Normal modes of the viscoelastic Earth, *Geophys. J. R. astr. Soc.,* **69**, 495–526.

APPENDIX A: VALIDITY OF CONTOUR-INTEGRAL REPRESENTATION FOR THE SOLUTION OF THE HELMHOLZ EQUATION ON A SPHERICAL MEMBRANE

Here we evaluate the validity of the numerical implementation of eq. (15) for individual spherical harmonic components and their horizontal spatial derivatives. Specifically we verify eq. (15) for functions of the form

$$\left\{1, \partial_\nu, \partial_\alpha, \partial^2_{\nu\alpha}, \partial^2_{\alpha\alpha}\right\}\left[X_l^N(\theta)\exp(iN\gamma)\right], \tag{A1}$$

where the Legendre function X_l^N is defined by

$$X_l^N(\theta) = (-1)^N \sqrt{\frac{2l+1}{4\pi}}\sqrt{\frac{(l-m)!}{(l+m)!}}\, P_l^N(\cos\theta), \tag{A2}$$

where θ and γ are to be considered functions of position $\hat{\mathbf{r}}'$ (Fig. 1), and ∂_α and ∂_ν are partial derivatives acting at $\hat{\mathbf{r}}'$ with respect to variables ν and α which measure distance towards due east and south, respectively. With N taking the values 0, 1, and 2, for a fixed l and two independent azimuthal functions for $N = 1, 2$, there are altogether 25 independent functions which must be considered. Note that the operator $\partial^2_{\nu\nu}$ applied to the spherical harmonic of degree l is equivalent to the operator $[-l(l+1) - \partial^2_{\alpha\alpha}]$ by virtue of the Helmholz equation. In order to evaluate the functions given in eq. (A1) with eq. (15), one requires up to third horizontal spatial derivatives of a spherical harmonic function evaluated on the contour C, that is, the additional differentiations $\partial^3_{\nu\alpha\alpha}$ and $\partial^3_{\alpha\alpha\alpha}$ applied to the Legendre functions, which results in 10 additional functions (the values of which are needed only on C). Analytic expressions have been derived and numerically implemented for the 35 functions generally required to evaluate the 25 functions in eq. (A1).

Supplementary Figs S5 to S9 show a comparison of the 25 functions of eq. (A1) with their representation by eq. (15) for degree $l = 1210$. The Legendre functions are defined with respect to an arbitrary pole shown in the figures. These comparisons validate eq. (15) and hence the employed analytic expressions for the 35 required

functions. Since these expressions are formulated in terms of general solutions of the Helmholz equation (eq. 14), they are equally applicable to a superposition of solutions, that is, $\Phi_j^1(\hat{\mathbf{r}}; s)$ as given in eq. (13).

SUPPLEMENTARY MATERIAL

The following supplementary material is available for this article: The supplementary material contains Figs S1–S9.

Figure S1. Radial functions $U(r)$, $V(r)$, and $W(r)$ associated with the highest 15 static modes of degree $l = 2000$ on a homogeneous elastic sphere (see Section 4.1): modes 1–5.
Figure S2. Continuation of Fig. S1: modes 6–10.
Figure S3. Continuation of Fig. S1: modes 11–15.
Figure S4. Continuation of Fig. S1: modes 16–20.
Figure S5. (right-hand side) Values of the 25 spherical harmonic functions given in eq. (A1) over a 1.4×1.4 squared geocentric de-gree area on the unit sphere, for $l = 1210$. (left-hand side) Contour integral representation of the same spherical harmonic functions using eq. (15), the contour being a small circle of radius 2.18 geo-centric degrees centred on the middle of the plotted area. The pole of the spherical harmonics is indicated in all plots with a triangle.
Figure S6. Continuation of Fig. S5.
Figure S7. Continuation of Fig. S5.
Figure S8. Continuation of Fig. S5.
Figure S9. Continuation of Fig. S5.

This material is available as part of the online article from: http://www.blackwell-synergy.com/doi/abs/10.1111/j.1365-246X.2007.03666.x
(this link will take you to the article abstract).